Flexural rigidity of the Basin and Range–Colorado Plateau–Rocky Mountain transition from coherence analysis of gravity and topography

Anthony R. Lowry and Robert B. Smith

Department of Geology and Geophysics, University of Utah, Salt Lake City

Abstract. Stochastic inversion for flexural loads and flexural rigidity of the continental elastic layer can be accomplished most effectively by using the coherence of gravity and topography. However, the spatial resolution of coherence analysis has been limited by use of two-dimensional periodogram spectra from very large ($> 10^5$ km^2) windows that generally include multiple tectonic features. Using a two-dimensional spectral estimator based on the maximum entropy method, the spatial resolution of flexural properties can be enhanced by a factor of 4 or more, enabling more detailed analysis at the scale of individual tectonic features. This new approach is used to map the spatial variation of flexural rigidity along the Basin and Range transition to the Colorado Plateau and Middle Rocky Mountains physiographic provinces. Large variations in flexural isostatic response are found, with rigidities ranging from as low as 8.7×10^{20} N m (elastic thickness $T_e = 4.6$ km) in the Basin and Range to as high as 4.1×10^{24} N m ($T_e = 77$ km) in the Middle Rocky Mountains. These results compare favorably with independent determinations of flexural rigidity in the region. Areas of low flexural rigidity correlate strongly with areas of high surface heat flow, as is expected from the contingence of flexural rigidity on a temperature-dependent flow law. Also, late Cenozoic normal faults with large displacements are found primarily in areas of low flexural rigidity, while deformation fronts of Mesozoic/Tertiary overthrusts occur 0 to 100 km east of the low-rigidity region. The highest flexural rigidity is found within the Archean Wyoming craton, where evidence suggests that deeply rooted cratonic lithosphere may play a role in determining the distribution of tectonism at the surface.

Introduction

The concept of isostasy proposes that the Earth is in hydrostatic equilibrium at depth, requiring topography to be compensated by lateral variations in crustal thickness [*Airy*, 1855] or crustal density [*Pratt*, 1855]. Flexural isostasy is an extension of the concept in which topography is supported partly by deflection of density discontinuities in Airy isostatic fashion and partly by stresses in a strong elastic layer overlying a weak ductile zone [*Barrell*, 1914; *Gunn*, 1943]. Flexural isostasy is modeled from theory of elastic plate flexure, governed by the fourth-order partial differential equation [e.g., *Turcotte and Schubert*, 1982]:

$$\nabla^2 \cdot \left(D \nabla^2 w \right) + P \nabla^2 w + \Delta \rho g w = q \tag{1}$$

where w is vertical deflection of the plate, $\Delta \rho$ is the density difference for material above and below the plate, g is gravitational acceleration, P is horizontal force (per unit length), and q is vertical stress applied to the plate. Thus flexural isostasy is parameterized by the resistance to bending or flexural rigidity D of the elastic layer.

An improved understanding of the Earth's isostatic behavior is desirable for a variety of applications. Investigators call upon isostasy to explain fault geometry in extensional ter-

rains [*Buck*, 1988; *Wernicke and Axen*, 1988], as well as the plateau-like expression of orogens [*Bird*, 1991]. Isostatic response is essential to our understanding of basin formation in a variety of tectonic settings [e.g., *McKenzie*, 1978; *Watts and Steckler*, 1981; *Jordan*, 1981]. Isostatic corrections to Bouguer gravity anomaly maps benefit from use of the true relationship between gravity and topography [e.g., *McNutt*, 1983] rather than the simplistic Airy approximation to isostatic behavior. *Watts and Ribe* [1984] suggest that if the Earth's isostatic behavior is constrained, its effects can be removed from geoid data to achieve a clearer picture of mantle convection processes.

Moreover, estimates of flexural rigidity contribute directly to our understanding of the evolution and mechanical behavior of the lithosphere. Observations of flexural rigidity (expressed in terms of an equivalent effective elastic thickness, T_e) were pointed to by *Watts* [1978] as an affirmation of the thermomechanical plate-cooling model for oceanic lithosphere. Subsequent evaluation of perturbational elastic thickness estimates have helped to illuminate anelastic behavior [*McNutt and Menard*, 1982] and stress accumulation [*Wessel*, 1992] in the oceanic elastic layer. Determinations of flexural rigidity should provide similar insights into the formation, evolution, and seismic properties of the continental lithosphere.

This discussion will first describe a new stochastic inversion for flexural rigidity of the elastic layer using a maximum entropy-based approach to coherence estimation. The method is then demonstrated by application to the tectonically important transition from the actively extending Basin and Range to

the relatively stable Colorado Plateau and Rocky Mountains physiographic provinces in the western United States. Estimates of flexural rigidity are compared to relevant geologic and geophysical information from the area and are found to be strongly correlated with patterns of heat flow and tectonism.

Coherence Method for Estimation of Flexural Rigidity

Flexural rigidity is estimated by assuming a model that describes loading of the elastic layer and then comparing topography (or bathymetry) to gravitational potential (in the form of a free air, Bouguer, or geoid anomaly) to solve for the loads and the load response. One common methodology compares the observed flexural response to an "obvious" loading process with a modeled response for various assumptions of flexural rigidity. Examples of obvious loading processes include seamounts [e.g., *Walcott*, 1970a] and plate bending at subduction zones [e.g., *Caldwell et al.*, 1976] in the case of the oceanic elastic layer. Flexural rigidity of the continental elastic layer is determined from loading by sedimentary basins [e.g., *Haxby et al.*, 1976], Pleistocene lakes [e.g., *Walcott*, 1970b], and mountain ranges formed by continental collisions [e.g., *Karner and Watts*, 1983; *Lyon-Caen and Molnar*, 1983]. Unfortunately, the paucity of sites in which such specific loading processes are found precludes the use of these techniques for systematic mapping across large areas.

The admittance and coherence techniques [*Lewis and Dorman*, 1970; *Forsyth*, 1985] compose another class of methods that exploit the stochastic relationship between gravity and topography signals to determine flexural response. Because sinusoids are eigenfunctions of the differential operator (1) that governs plate flexure, the Fourier amplitudes of topography $H(k)$ and of the complete Bouguer gravity anomaly $B(k)$ can be linearly related by

$$B(k) = Q(k)H(k) \qquad (2)$$

[*Dorman and Lewis*, 1970], where Q is the linear isostatic response function (or admittance) and k is the two-dimensional wavenumber:

$$k = \left(\frac{2\pi}{\lambda_x}, \frac{2\pi}{\lambda_y}\right). \qquad (3)$$

When flexural rigidity is estimated from the admittance function, the model chosen to parameterize $Q(k)$ is critically important. Early investigations assumed local or Airy compensation of surface topography and inverted for the compensating density anomalies at depth [*Lewis and Dorman*, 1970; *Dorman and Lewis*, 1972]. The Airy isostatic parameterization was superseded by that of an isostatic response to topographic loading at the top of an elastic plate [e.g., *McKenzie and Bowin*, 1976; *Banks et al.*, 1977]. *Lewis and Dorman* [1970] recognized, however, that much of the surface expression of topography represents the Earth's response to density variations at depth rather than loads emplaced upon the surface. The further recognition that flexural rigidity would be systematically underestimated if interior or bottom loading contributed to a flexural response modeled as a plate loaded at the top provided the impetus for development of the coherence method by *Forsyth* [1985].

The coherence function is the square of the correlation coefficient between two signals, a positive number ranging between zero and one. Coherence can be thought of as a measure of the fraction of the gravity field that can be predicted from the topography using (2). Coherence has a strong dependence on flexural rigidity (Figure 1) and so is appropriate for use in its estimation. The coherence function is estimated from the autopower spectra of topography $P_{hh}(k)$ and gravity $P_{bb}(k)$ and the cross-power spectrum of the two signals, $P_{hb}(k)$, by

$$\hat{\gamma}_{hb}^{2}(k) = \frac{|P_{hb}(k)|^{2}}{P_{hh}(k)P_{bb}(k)}. \qquad (4)$$

In practice, power spectra are averaged to reduce bias introduced by uncorrelated noise processes. Averaging of the two-dimensional spectra, denoted by angle brackets, is performed within annular wavenumber bins based on the assumption that flexural response is isotropic. In that case coherence is one-dimensional and expressed as

$$\hat{\gamma}_{hb}^{2}(k) = \frac{|\langle P_{hb}(k)\rangle|^{2}}{\langle P_{hh}(k)\rangle \langle P_{bb}(k)\rangle}. \qquad (5)$$

where k is the modulus of the two-dimensional wavenumber, $k = |k| = (k_x^2 + k_y^2)^{-1/2}$.

Coherence analysis of isostatic response [*Forsyth*, 1985] first uses the observed admittance and an assumed flexural rigidity to solve for load structure in the Earth. Fourier amplitudes of the topography H and the Bouguer gravity B are used to solve algebraically for the amplitudes of topography H_I and a subsurface load horizon W_I prior to flexural compensation (Figure 2b). Once the initial loads have been determined, the topography and gravity amplitudes can be deconvolved into their respective components, H_T and B_T due to surface loading and H_B and B_B due to interior loading of the elastic plate (Figure 2c). The coherence of the deconvolved signals is then estimated by assuming the surface and subsurface loading processes are statistically uncorrelated: i.e., they have some ran-
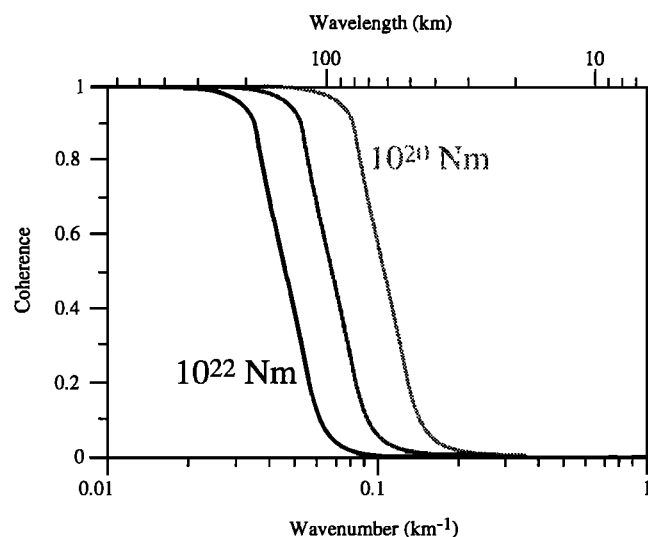

Figure 1. Coherence of gravity and topography at specific wavelengths is strongly dependent on flexural rigidity and so is well suited for use in its estimation. After *Forsyth* [1985].
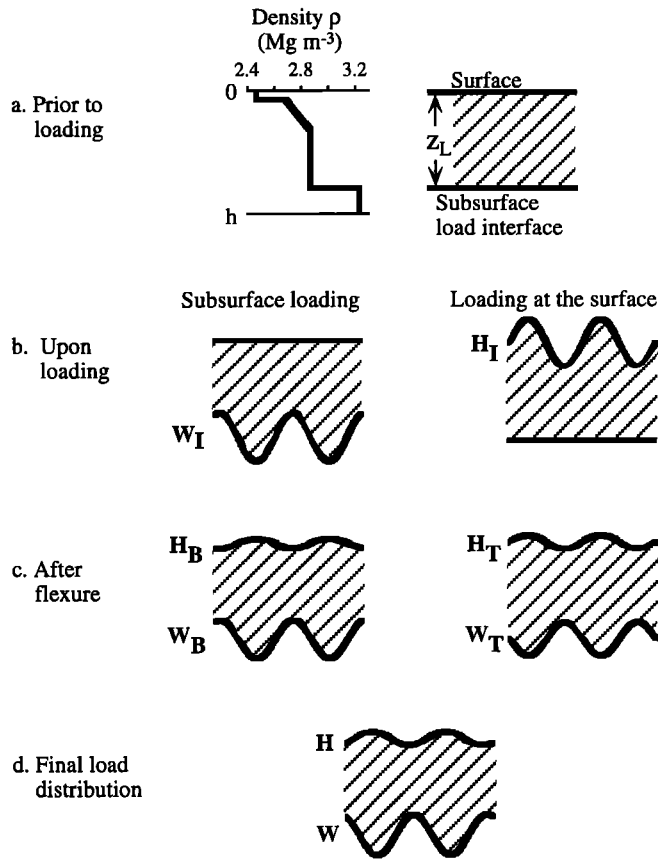
[e.g., *Kay*, 1988]. Windowing effects can be reduced by using a data sequence that is very large relative to the wavelengths of interest, and so previous researchers [e.g., *Bechtel*, 1989] have chosen to mirror the data (i.e., repeat the data symmetrically across a window edge). However, the wavelengths of transition from high to low coherence are very long, ~100 to 800 km in the North American continent [*Bechtel* et al., 1990], and even when data are mirrored, the spectral properties must be computed for very large geographic areas, of order 10^5 to 10^6 km^2, to be accurately resolved. Coherence analysis assumes uniform flexural rigidity, so the flexural rigidity which gives the best fit to the coherence function will be a weighted average of the rigidity throughout the sampled region. As a result, periodogram coherence analysis has not been useful for smaller-scale tectonic features or at boundaries between tectonic features where elastic strength may vary significantly over short distances.

To test the periodogram coherence estimator, we generated a pair of data sets with known coherence. We first Fourier transformed a large area (1600 by 1200 km) of topographic data from the western United States to the frequency domain. We then generated synthetic "gravity" amplitudes B_s using an assumed coherence function γ_a^2 by adding random-phase noise with amplitude N to the topographic amplitudes, where

$$| N(k) |^2 = | H(k) |^2 \frac{1 - \gamma_a^2(k)}{\gamma_a^2(k)} \qquad (7)$$

The synthetic gravity amplitudes were then inverse Fourier transformed to the spatial domain, and a smaller data window was extracted from the center of each data set for estimation of the coherence using (5). In spite of the use of mirrored data, the periodogram method used by previous researchers provides a poor estimate of coherence when the data window is small (Figure 3a). Figure 3a, like all subsequent figures displaying coherence functions, superimposes coherence estimates calculated for several realizations of the spectral averaging operation, corresponding to different numbers n of annular wavenumber bins, $n = 20$ to 30, to indicate variance. The periodogram coherence estimate exhibits a great deal of scatter. Also, the true coherence function changes from zero to one at wavelengths close to the dimension of the data window, and that transition is virtually unresolved. Increasing the size of the data set improves the periodogram estimate of coherence (Figure 3b), but the method still yields a poor approximation to the true coherence function at transitional wavelengths. A still larger data set would further improve the coherence function, but given the nonstationarity of flexural properties, it is preferable to minimize the size of the data sequence.

Maximum Entropy Spectral Estimation

Several alternative spectral estimators have been developed that attempt to reduce or remove the effects of windowing of data [e.g., *Kay and Marple*, 1981]. Maximum entropy spectral estimation (MESE) is one such method that has enjoyed a measure of success for a wide range of applications in science and engineering [e.g., *Smith and Grandy*, 1985]. The motivation for MESE is similar to that for mirroring: namely, to reduce the effects of data windowing via a reasonable extrapolation of the information. Specifically, MESE seeks to describe a
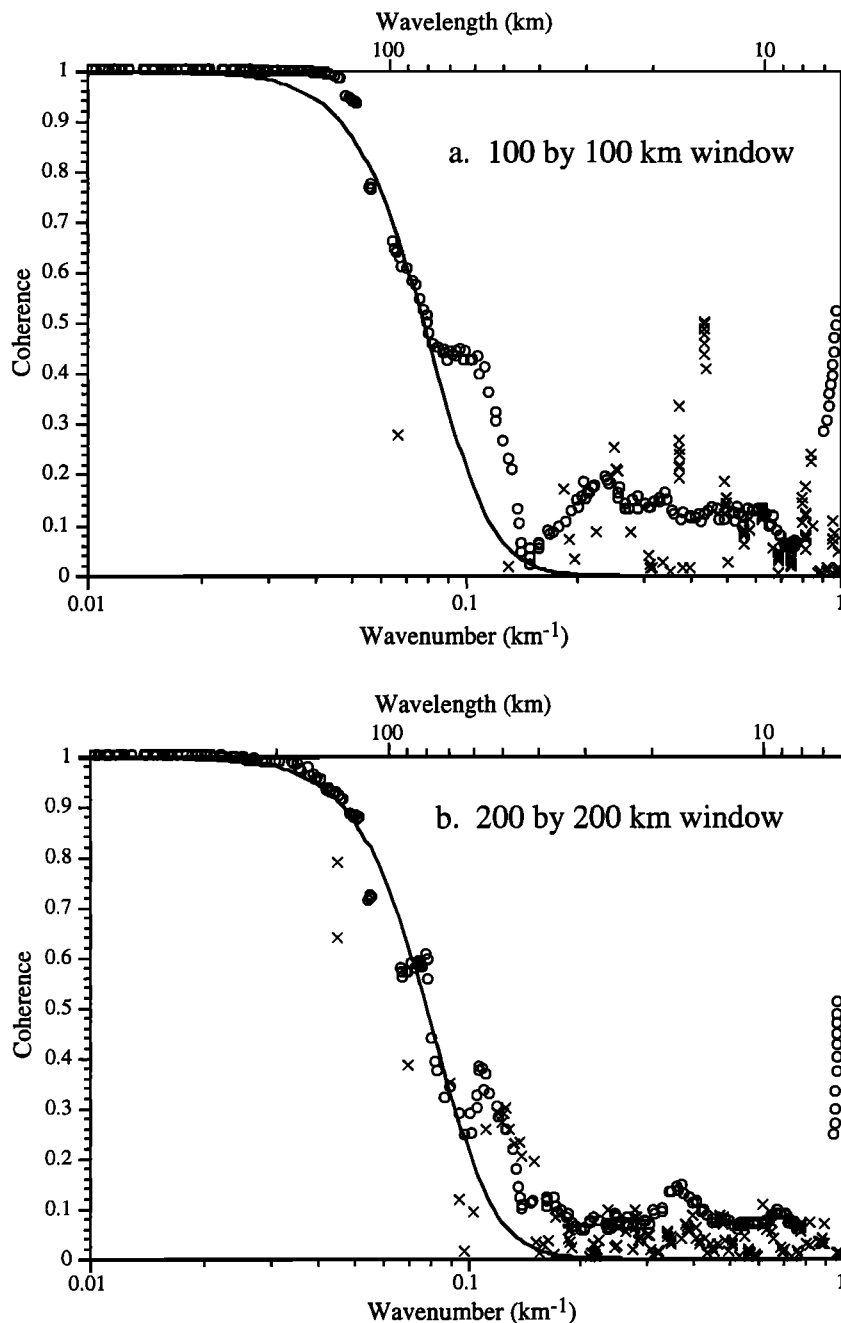

Figure 2. Fourier isostatic model [after *Forsyth*, 1985]. (a) An elastic layer of thickness h, having arbitrary density variation with depth. (b) Sinusoidal loading with Fourier amplitude H_I is applied at the top; loading with amplitude W_I occurs at depth z_L. (c) Flexure results in topographic amplitudes H_T due to surface loading and H_B due to subsurface loading. Deflections of the subsurface load interface have amplitude W_T and W_B, respectively. (d) Observed topography H and internal deflection W sum the surface and subsurface responses.

dom difference in phase. In that case, the predictive coherence $\hat{\gamma}_{hb}^2(k)$ is calculated from

$$\hat{\gamma}_{hb}^2(k) = \frac{\left| \left\langle P_{hb}^{tt}(k) + P_{hb}^{bb}(k) \right\rangle \right|^2}{\left\langle P_{hh}^{tt}(k) + P_{hh}^{bb}(k) \right\rangle \left\langle P_{bb}^{tt}(k) + P_{bb}^{bb}(k) \right\rangle} \qquad (6)$$

where superscripts t and b denote top and interior (or "basal") loading, respectively. The predictive coherence function (6) is estimated for several different assumed flexural rigidities and then compared to the observed coherence (4) to determine the flexural rigidity that best models the load response of the elastic layer.

Periodogram Spectral Estimation

Previous investigations of flexural rigidity using the coherence method have employed a classical Fourier transform technique, the periodogram method, to estimate power spectra. Unfortunately, the periodogram is plagued by spectral bias and leakage resulting from the implicit windowing of finite data

Figure 3. Coherence of synthetic data. Solid line is the coherence function used to generate the data. Periodogram coherence is indicated by crosses; maximum entropy-based coherence is indicated by open circles. (a) Estimates for a 100x100 km window. (b) Estimates for a 200x200 km window.

power spectrum exhibiting minimum bias, corresponding to the Fourier transform of the extrapolated correlation function having maximum entropy [*Burg*, 1975].

The *Burg* [1975] formulation of MESE, commonly used for one-dimensional signals, is equivalent to autoregressive spectral estimation [e.g., *Kay and Marple*, 1981], and the two follow a similar procedure. In each case, "extrapolation" of the correlation function to larger lags is implicit rather than explicit. However, the two-dimensional extension of Burg's one-dimensional maximum entropy formulation requires solution of a large system of nonlinear equations. Fortunately, the implied computational nightmare can be avoided by reformu-

lating the problem in terms of an iterative algorithm constrained such that the power spectrum will converge to the maximum entropy solution [*Lim and Malik*, 1981].

The problem is posed as follows: given a process $h[m,n]$ with correlation function $r_{hh}[m,n]$ that is known or estimated over some windowed area A, determine the extrapolation of the known correlation function having maximum entropy. The extrapolated correlation should of course equal the known correlation within A:

$$\hat{r}_{hh}[m,n] = F^{-1}\left\{\hat{P}_{hh}(k_1,k_2)\right\} = r_{hh}[m,n] \text{ for } [m,n] \in A \qquad (8)$$

where $F^{-1}\{\cdot\}$ represents the inverse Fourier transform operator and $\tilde{r}_{hh}[m,n]$ is the extrapolated correlation function. It can be shown [e.g., *Smylie et al.*, 1973] that if the process is Gaussian, the Shannon entropy E is given by

$$E = \int_{-\pi}^{\pi} \int_{-\pi}^{\pi} \log\left[\hat{P}_{hh}(k_1,k_2)\right] dk_1 dk_2. \qquad (9)$$

Maximization of (9) has the trivial solution

$$F^{-1}\left\{\frac{1}{\hat{P}_{hh}(k_1,k_2)}\right\} = 0 \text{ for}[m,n] \notin A. \qquad (10)$$

Lim and Malik [1981] develop an iterative MESE algorithm based on the constraints (8) and (10), which we have adapted to the determination of autopower and crosspower spectra of gravity and topography for coherence analysis. However, it is important to note that whereas the autospectra are maximum entropy spectra, in the case of a crosspower spectrum the application of the constraint (10) does not correspond to maximization of entropy (a proof may be found in Appendix A of *Lowry* [1994]), and the information quantity that is being minimaxed has not yet been identified. Hence this study does not actually employ a maximum entropy coherence estimator; although based on the maximum entropy method, this is an ad hoc coherence estimation technique.

The coherence function was reduced to one dimension via averaging within annular wavenumber bins using

$$\hat{\gamma}_{hb}^2 = \left| \left\langle \frac{(P_{hb})^2}{P_{hh}P_{bb}} \right\rangle \right| \qquad (11)$$

in place of the averaging scheme given by (6), simply because (11) was found to perform better in tests of the method. The resulting coherence functions exhibit a positive bias at wavelengths for which the true coherence approaches zero (Figure 3), perhaps because maximum entropy spectra tend to represent noise processes poorly. Nevertheless, the maximum entropy-based estimates of coherence used in this study improve greatly upon those determined using the periodogram method for the same synthetic data, particularly at the important wavelengths of transition.

Other Adjustments

In addition to the alternative choice of spectral estimator, the following minor modifications of previous practice are made for this study: (1) the data are not mirrored prior to stochastic analysis; (2) surface and subsurface load responses are deconvolved within a much larger data segment than that for which power spectral estimation is performed; and (3) relatively complex one-dimensional density profiles of the elastic layer, as inferred from Nafe-Drake regression of P wave velocities from seismic refraction profiles, are included in the isostatic model.

Mirroring of Data

Mirroring of data prior to calculation of Fourier amplitudes (which are utilized in calculation of periodogram spectra as well as deconvolution of surface and subsurface load distributions) deserves some discussion. This practice was first used by *Lewis and Dorman* [1970] and is still commonly employed by researchers using periodogram spectra [e.g., *Blackman and Forsyth*, 1991] to reduce the spectral bias and leakage that result from finite data. Figure 4a depicts the periodogram coherence estimated from mirrored and unmirrored synthetic data, indicating that while the coherence functions are differently biased at long wavelengths, the estimates are comparably accurate.

A more intriguing dissimilarity is apparent when mirroring is applied to real gravity and topography data (Figure 4b). Here the greatest difference between the mirrored and unmirrored coherence functions is at short wavelengths, where the unmirrored coherence actually increases with decreasing wavelength instead of leveling off near zero. This feature is an artefact of the homogeneous reduction density used to calculate the Bouguer anomaly. While an average density is adequate for Bouguer reduction at long wavelengths, locally contiguous bodies which deviate significantly from the reduction density and are exposed in surface topography will generate Bouguer "anomalies" which will correlate with topography because the reduction density was unrepresentative at that location [e.g., *Black*, 1992]. The coherence increases with decreasing wavelength because the likelihood that such bodies will be continuously represented at the surface decreases with increasing scale. When the data are mirrored, however, a skein of incoherent noise is introduced into the spectra which is apparently of large enough amplitude to dominate the coherency of signals at short wavelengths.

Despite the difference in coherence functions, mirrored data yield a virtually identical value for the best fit flexural rigidity as unmirrored data. For example, the coherence functions in Figure 4b correspond to rigidities of 2.9×10^{21} N m and 2.6×10^{21} N m for the mirrored and unmirrored cases, respectively. To arrive at these estimates, the same type of Fourier amplitudes (i.e., mirrored or unmirrored) were used to determine the predictive coherence functions as were used to estimate the observed coherence. Hence the estimates of flexural rigidity are virtually identical because the bias and noise processes introduced in the predictive coherence functions were similar to those in the observed coherence in each case. The artificial noise processes introduced by mirroring cause severe degradation of maximum entropy-based coherence functions, however (Figure 5), so data were not mirrored for this study.

Windowing for Deconvolution

Deconvolution of surface and subsurface load responses is performed in a relatively large window for this study. Spectral bias and leakage have been greatly reduced in the observed coherence function by using a maximum entropy-based method, so it would be counterproductive to introduce these effects into the predictive coherence function by performing the deconvolution within a small data window. Instead the deconvolution uses the amplitudes from a much larger data segment (at least 12 times the area for which power spectra are estimated). The amplitudes are then inverse transformed to the spatial domain, and the corresponding subset of the deconvolved data is selected for use in estimating the predictive coherence function.

Density Model From P Wave Velocities

The assumed density variation with depth in the elastic layer was also modified. Previous investigations have incor-
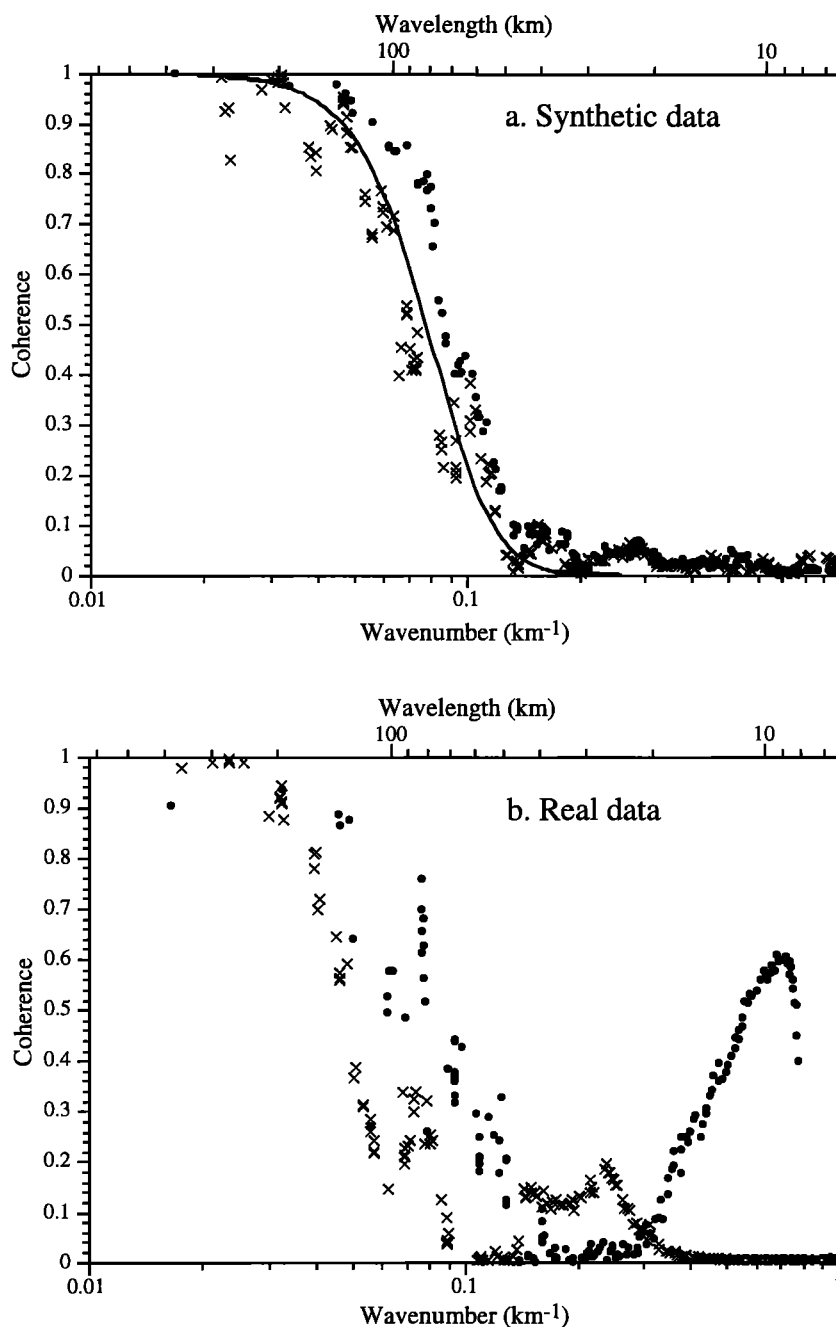
Figure 4. Mirrored and unmirrored periodogram coherence for a 600x600 km window. (a) For synthetic data, mirroring (crosses) produces slight negative bias; unmirrored data (solid circles) are positively biased at transitional wavelengths. (b) Unmirrored coherence is high at short wavelengths for real data.

porated geologically reasonable density values for one or at most two layers over a half-space, with depths inferred either from the gravity power spectrum or from seismic data. However, the deconvolution of gravity and topography can be accomplished using any arbitrary one-dimensional density model via the relations described in the appendix. Density distributions for this study are approximated using a Nafe-Drake regression of P wave velocities [*Ludwig et al.*, 1970] from crustal seismic refraction surveys in the area of interest. The Nafe-Drake relationship may be poorly suited to the prediction of density structures (i.e., lateral variations in density, see, for example, *Barton* [1986]); however, in the modeling

undertaken here the functional dependence is on vertical changes in density $\Delta\rho$ and the depth z at which they occur:

$$\int_0^h \frac{d\rho}{dz} \exp(-kz)dz.$$

Jones et al. [1992] suggest that variations in density for a given P wave velocity are primarily the result of variations in the mean atomic number of crustal rocks; in which case a Nafe-Drake density profile should be representative (and probably
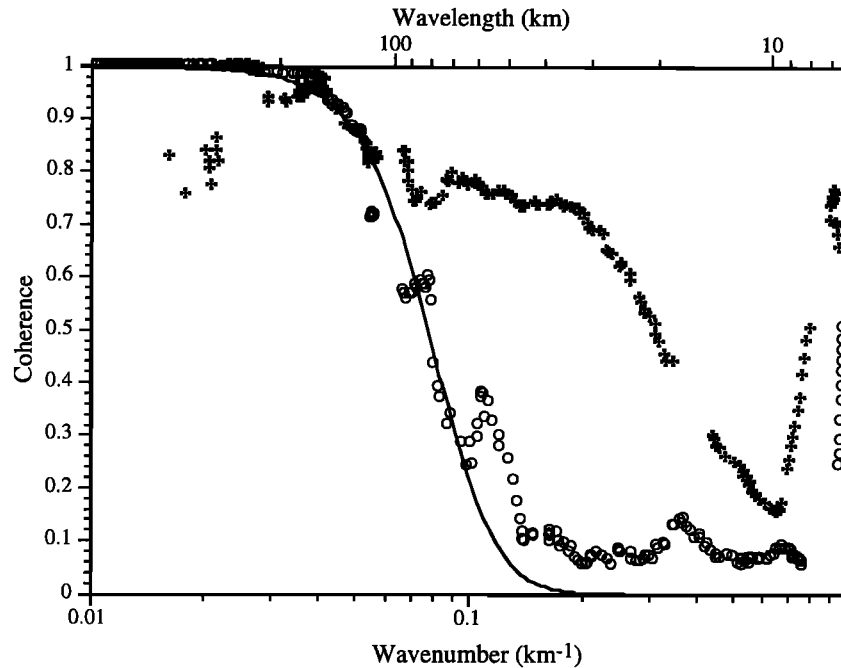
Figure 5. Maximum entropy coherence functions from unmirrored data (open circles) and mirrored data (crosses) for a 200x200 km window. Solid line is true coherence.

will give the most accurate profile from among the geophysi-cal options available). Velocities from seismic refraction pro-files are preferred over those from reflection data because re-fraction averages out lateral variations in velocity structure, yielding a more representative one-dimensional distribution. The density modification is ultimately a minor improvement, however: tests indicate that complicating the density structure as well as changing the subsurface load depth change the re-sulting estimate of flexural rigidity by no more than about a factor of 2 (corresponding to a factor of 1.3 change in elastic thickness).

Limitations of the Method

As with all Earth models, the coherence method is subject to the validity of its implicit assumptions. Included among these are the fundamental approximation of the behavior of the elas-tic layer as that of a perfectly elastic plate, incorporation of a thin plate approximation to flexural behavior, assumption of a crustal density variation with depth, and restriction of load-ing processes to either the surface or a single subsurface den-sity interface. However, it is expected (based on empirical tests and other arguments, e.g., *Forsyth* [1985], *Bechtel et al.* [1987], and *Bechtel* [1989]) that these assumptions introduce acceptably small errors into the estimate of rigidity.

On the other hand, the supposition that surface and subsur-face loading processes are uncorrelated is critically important. *Macario et al.* [1992] report that the coherence method under-estimates flexural rigidity if surface and subsurface loads are strongly correlated. One can envision circumstances (such as the combination of volcanic and thermal loading in volcanic provinces) in which such correlation may indeed be expected. Hence the possible bias of coherence analysis should be heeded, particularly given that the possibility of load correla-tion may increase if one samples fewer independent geologic features in smaller data windows.

The coherence estimator employed here is based on a maxi-mum entropy spectral estimator, which also has some minor limitations. The appropriate probability density distributions for gravity and topography processes are not explicitly solved for; rather the entropy description (9) implicitly assumes a Gaussian (corresponding to the most entropic [e.g., *Jaynes*, 1985]) probability density distribution. The latter methodol-ogy is commonly referred to as a Gibbsian approach. Some minor problems have been recognized in other Gibbsian max-imum entropy methods such as the Burg algorithm, including the exhibition of spurious peaks, spectral line splitting, and phase dependence of sinusoidal peak location [e.g., *Kay and Marple*, 1981]. *Malik and Lim* [1982] observe similar diffi-culties with the two-dimensional algorithm used in this study. It is unclear how (or if) these problems may translate into the coherence estimate, particularly given the ad hoc nature of the cross-power spectral estimator. Nevertheless, the maximum entropy-based estimates of coherence afford a clear improve-ment over periodogram estimates for the topographic and gravity data used to estimate flexural rigidity (Figure 3).

Flexural Properties of the Basin and Range–Colorado Plateau–Rocky Mountain Transition

Coherence analysis was applied to the eastern Basin and Range province at its transition to the Middle Rocky Mountains and northwestern Colorado Plateau physiographic provinces (Plate 1). Flexural rigidity depends strongly on the composition and tectonic evolution of the lithosphere, and these provinces reflect very different formative and tectonic histories that are likely to manifest as abrupt variations in lithospheric character. The Middle Rocky Mountains physio-graphic province lies within the Wyoming isotopic age province, a > 2500-m.y.-old cratonic province that is approx-imately defined by surface expression of basement rocks with K-Ar biotite ages greater than 1.4 b.y. [*Condie*, 1981]. The
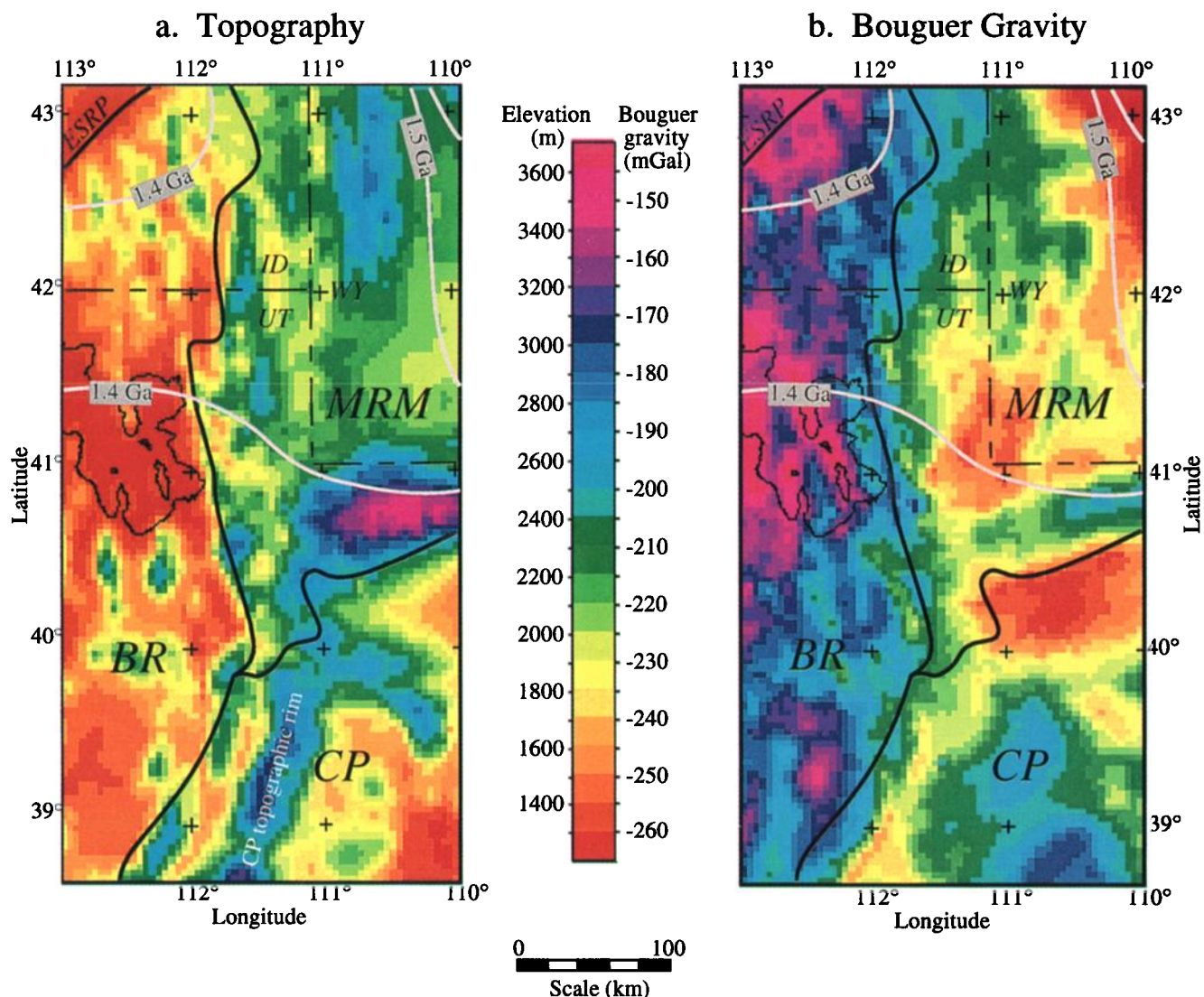
a. Topography

b. Bouguer Gravity

Plate 1. The data used for this study: (a) Topography. (b) Complete Bouguer gravity. Grey lines are K-Ar isotopic age contours of the Archean Wyoming craton; physiographic province abbreviations are CP, Colorado Plateau; BR, Basin and Range; MRM, Middle Rocky Mountains; ESRP, eastern Snake River Plain.

Colorado Plateau is thought to have originated when island arc material accreted to the Wyoming province circa 1800–1600 Ma [*Karlstrom and Houston*, 1984], but a lack of surface exposures of Precambrian basement hinders confident assessment of the age and genesis of the province. The modern Basin and Range was initially the site of miogeoclinal deposition subsequent to a late Precambrian rifting event.

The tectonic history of the Cordillera is complex and likewise varies according to province. During the Paleozoic and up to Jurassic time, a hinge line separated the cratonic shelf of the Middle Rocky Mountains–Colorado Plateau from the passive margin basin deposition in the Basin and Range [*Burchfiel and Davis*, 1975; *Stewart*, 1978]. From late Jurassic to Eocene, western North America experienced Andean-type tectonism associated with low-angle subduction of the Farallon plate [e.g., *Lipman et al.*, 1972]. Exact timing varies from place to place, but within the study area, contraction occurred primarily in Cretaceous-Tertiary time (~90–50 Ma [e.g., *Wernicke et al.*, 1987]). East-west shortening in the Basin and Range was accommodated by low-angle reverse

faults and associated folding that inverted the miogeoclinal structure during the Sevier and Laramide orogenies [e.g., *Wernicke et al.*, 1987]. In the Middle Rocky Mountains, contraction was expressed in the form of higher-angle reverse faults and monoclines, generating broad basins and basement uplifts during the Laramide. Contraction of the Colorado Plateau in Laramide time occurred principally in the form of monoclinal structures. Tectonism reversed to extension in the Basin and Range beginning around Oligocene (~30 Ma [e.g., *Anderson*, 1989]) and continuing to the present day. Normal faults exhibiting significant displacement are generally restricted to the Basin and Range, but various indicators suggest the stress regime is currently extensional in the Colorado Plateau and Middle Rocky Mountains provinces as well [*Zoback and Zoback*, 1989].

The divergent histories of these provinces are reflected in their geophysical signatures. As observed from seismic refraction data, the Middle Rocky Mountains crust is about 40 km thick, and upper mantle compressional wave (P_n) velocity is in the range 7.9 to 8.0 km s^{-1} [e.g., *Smith et al.*, 1989]. The

Colorado Plateau also has ~40 km crustal thickness, but P_n velocity is 8.1 km s^{-1} [*Beghoul and Barazangi*, 1989]. Most of the Basin and Range has a 28–30 km thick crust with a 7.8 km s^{-1} P_n velocity, but interpretation of refraction data in the easternmost Basin and Range is ambiguous [*Smith et al.*, 1989]. Crustal thickness there has been modeled from 25 to 45 km, with corresponding P_n velocities of 7.4 to 7.9 km s^{-1}, respectively. Tomographic imaging of upper mantle P velocity from teleseismic travel time residuals [*Humphreys and Dueker*, 1994] generally indicates high velocity in the Middle Rocky Mountains and northern panhandle of Utah, intermediate velocity in the Colorado Plateau interior, and low velocity in the eastern Snake River Plain, eastern Basin and Range south of the Great Salt Lake, and around the Colorado Plateau periphery.

The topographic expression (Plate 1a) is dominated by relatively low, <1.5 km, average elevation in the easternmost Basin and Range and high, slightly >2.0 km, average elevation in the Middle Rocky Mountains. The regional Bouguer gravity field (Plate 1b) is negatively correlated with topography at province-wide scales, as is expected from the isostatic model. Interestingly, the Colorado Plateau exhibits higher, ~2.0 km, average elevation around its rim (for example, ~40–

60 km east of the Basin and Range boundary in Plate 1a) with lower, ~1.5 km, elevation in the province interior. Topographic features analogous to the Colorado Plateau rim are commonly found adjacent to continental rifts. These rift flank uplifts appear to be independent of the local uplift associated with normal faulting [e.g., *King and Ellis*, 1990] and have been modeled respectively as a flexural isostatic response to lithospheric necking [*Chery et al.*, 1992] and an erosional process which is concentrated by the flexural response to denudational unloading [*Tucker and Slingerland*, this issue].

Coherence analysis was applied to the companion topography and complete Bouguer gravity data sets (Plate 1) employed by *Simpson et al.* [1986] for development of an isostatic residual gravity map. The gravity is gridded at a 4 by 4 km spacing from similarly distributed measurements that were processed to remove outliers [e.g., *O'Hara and Lyons*, 1983]. The topography is an identically parameterized grid generated from 5 arc min data specifically for the purpose of tandem signal processing [*Simpson et al.*, 1986]. Flexural rigidity was estimated for 200x200 and 400x400 km windows with centers spaced 50 km apart, and rigidity estimates were then interpolated to a 10-km spacing for the purpose of contouring using a
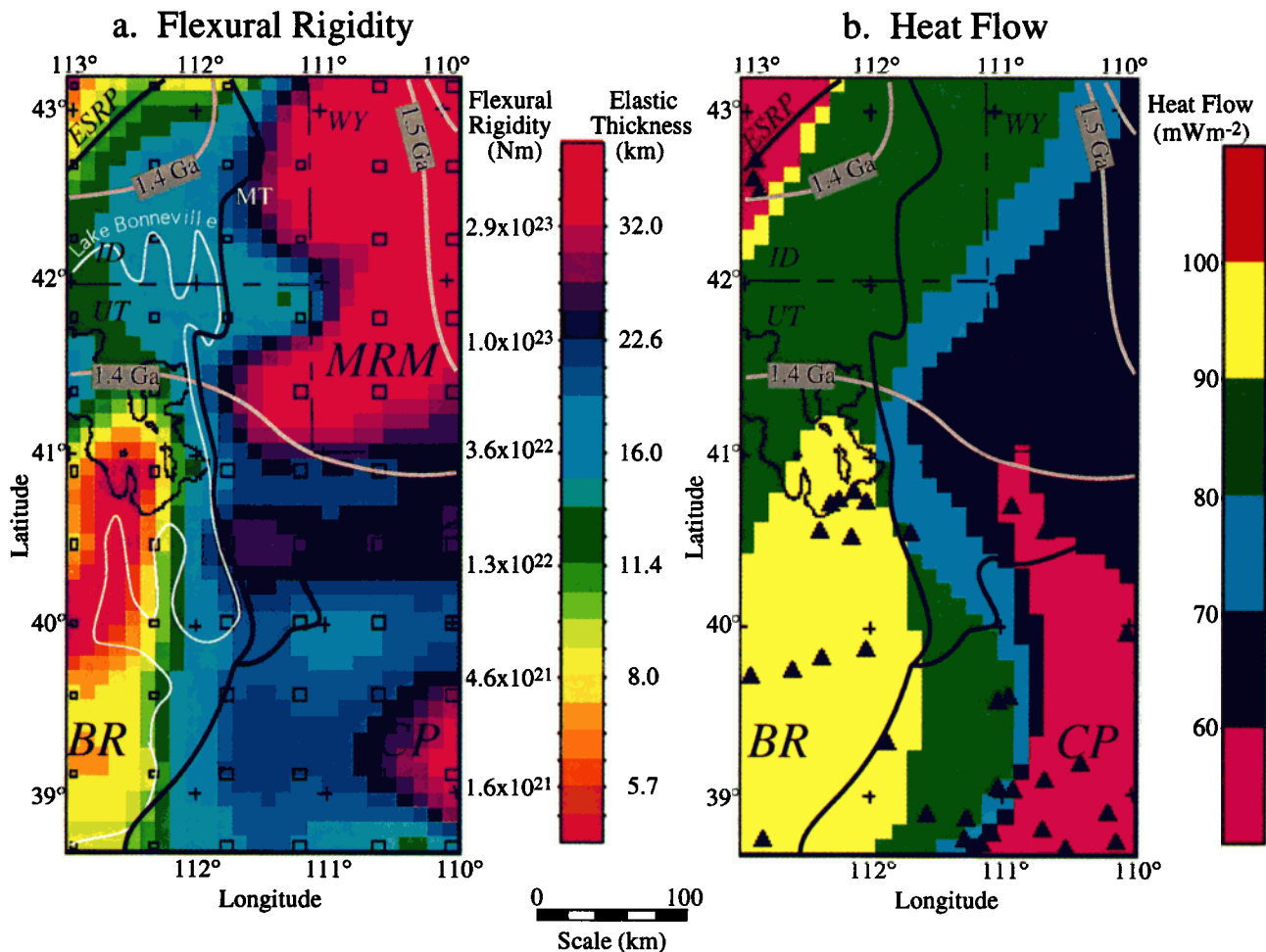

Plate 2. Flexural rigidity and regional surface heat flow. (a) Interpolated color contour of flexural rigidity. Contour interval varies logarithmically. Boxes are center locations of windows (larger boxes, 400x400 km windows; smaller boxes, 200x200 km windows). MT denotes palinspastic location of the Meade thrust modeled by *Jordan* [1981]; white contour approximates the highstand shoreline of Pleistocene Lake Bonneville. (b) Regional surface heat flow [*Blackwell and Steele*, 1992]. Solid triangles indicate constraining measurements. Age contours and province abbreviations are as in Plate 1.

minimum curvature algorithm. We note that the close spacing requires significant overlap of data windows for neighboring estimates of flexural rigidity, implying some smoothing of the rigidity distribution. In order to rigorously determine the resolution, the method should be applied to synthetic data with a known variation of rigidity, and we have not yet attempted such testing. However, we hope to demonstrate from comparison to geologic information that coherence analysis does indeed resolve changes in flexural strength at the spatial scales used in this study.

Flexural rigidity of the study area is presented in Plate 2a. Conversion to the equivalent effective elastic thickness T_e is also given, assuming a Young's modulus of 10^{11} Pa and Poisson's ratio 0.25. The P wave velocities that were used to constrain the density distribution are described in Table 1. We chose the shallowest first-order density/velocity discontinuity to serve as the subsurface load depth, because the downward continuation operation implicit in the load deconvolution is most stable for shallow depths. Examples of observed and best fit predicted coherence functions, as well as plots of residual error (the L_2 norm of observed minus predicted coherence), are given in Figure 6 for two locations.

The residual error of the coherence functions (Figure 7) is used to assess reliability of the coherence estimate. Where the best fit residual error significantly exceeds the standard deviation of the coherence estimates (~ 0.03), some failure of the modeling assumptions is indicated. The bulk of the misfit is likely to occur in areas where there is correlation of surface and subsurface load processes [*Macario et al.*, 1992], implying possible underestimation of rigidity at locations where residual error is high. Residual error functions are also used to assess standard error limits of the rigidity estimate, as defined by the range of flexural rigidities for which the difference between residual error and the global minimum of the residual error

function is less than a single standard deviation of the coherence estimate. Error limits determined in this manner are particularly useful for assessing whether a data window is large enough to completely resolve the transitional wavelengths of coherence: When the data window is too small, the error function flattens and the error range is unreasonably broad. Hence a 200x200 km window centered at the northern boundary of the Colorado Plateau province may exhibit an error range of 3×10^{22} to 1×10^{26} N m ($T_e = 15$ to 250 km), whereas the corresponding 400x400 km window has error limits at 2×10^{22} to 6×10^{23} N m ($T_e = 13$ to 41 km), indicating that the latter is a preferable size.

Very large variations in flexural isostatic response are observed within the 125,000 km^2 study area (Plate 2a). Estimates of rigidity range from as low as 8.7×10^{20} N m ($T_e = 4.6$ km) to as high as 4.1×10^{24} N m ($T_e = 77$ km). To place these values in perspective, consider that flexural rigidities reported for the oceanic elastic layer range from about 2×10^{20} N m ($T_e = 3$ km) for seamounts formed at mid-ocean ridges to around 3×10^{24} N m ($T_e = 70$ km) in the case of a few studies of very old (75 to 140 Ma) lithosphere at oceanic trenches (see, e.g., the compilation of *Wessel* [1992]). The *Bechtel et al.* [1990] coherence study of the North American continent, which assessed rigidity at scales of 400 km or more, documented rigidities ranging from 1×10^{21} N m ($T_e = 4.9$ km) in the Basin and Range to 2×10^{25} N m ($T_e = 123$ km) in the Canadian shield.

Large-scale variations of flexural rigidity broadly correspond to physiographic province (Plate 2a). The Basin and Range exhibits relatively low flexural rigidity of 8.7×10^{20} to 3.6×10^{22} N m ($T_e = 4.6$ to 16 km), with a mean rigidity of 9×10^{21} N m ($T_e = 10$ km) and median error limits 1×10^{21} to 4×10^{22} N m ($T_e = 5$ to 16 km). The northwestern part of the study area, within the eastern Snake River Plain volcanic

Table 1. Density Models Used to Constrain the Inversion

Layer	Eastern Basin and Range[a]			Western Middle Rocky Mountains[a]		
	Depth to Top, m	Velocity, m/s	Density, kg/m^3	Depth to Top, m	Velocity, m/s	Density, kg/m^3
1	0	3400	2280	0	4600	2470
2	1700	6000	2700	3000	5900	2680
3	8400	5500	2610	16000	6750	2870
4	14700	6500	2800	40000	7900	3230
5	24700	7400	3050	--	--	--

Layer	Eastern Snake River Plain[b]			Colorado Plateau[c]		
	Depth to Top, m	Velocity, m/s	Density, kg/m^3	Depth to Top, m	Velocity, m/s	Density, kg/m^3
1	0	3330	2270	0	3000	2210
2	1500	5210	2560	1700	6200	2740
3	5200	6130	2730	26000	6800	2880
4	10700	6510	2810	41000	7800	3190
5	18800	6800	2880	--	--	--
6	41500	7920	3240	--	--	--

[a]From *Braile et al.* [1974].
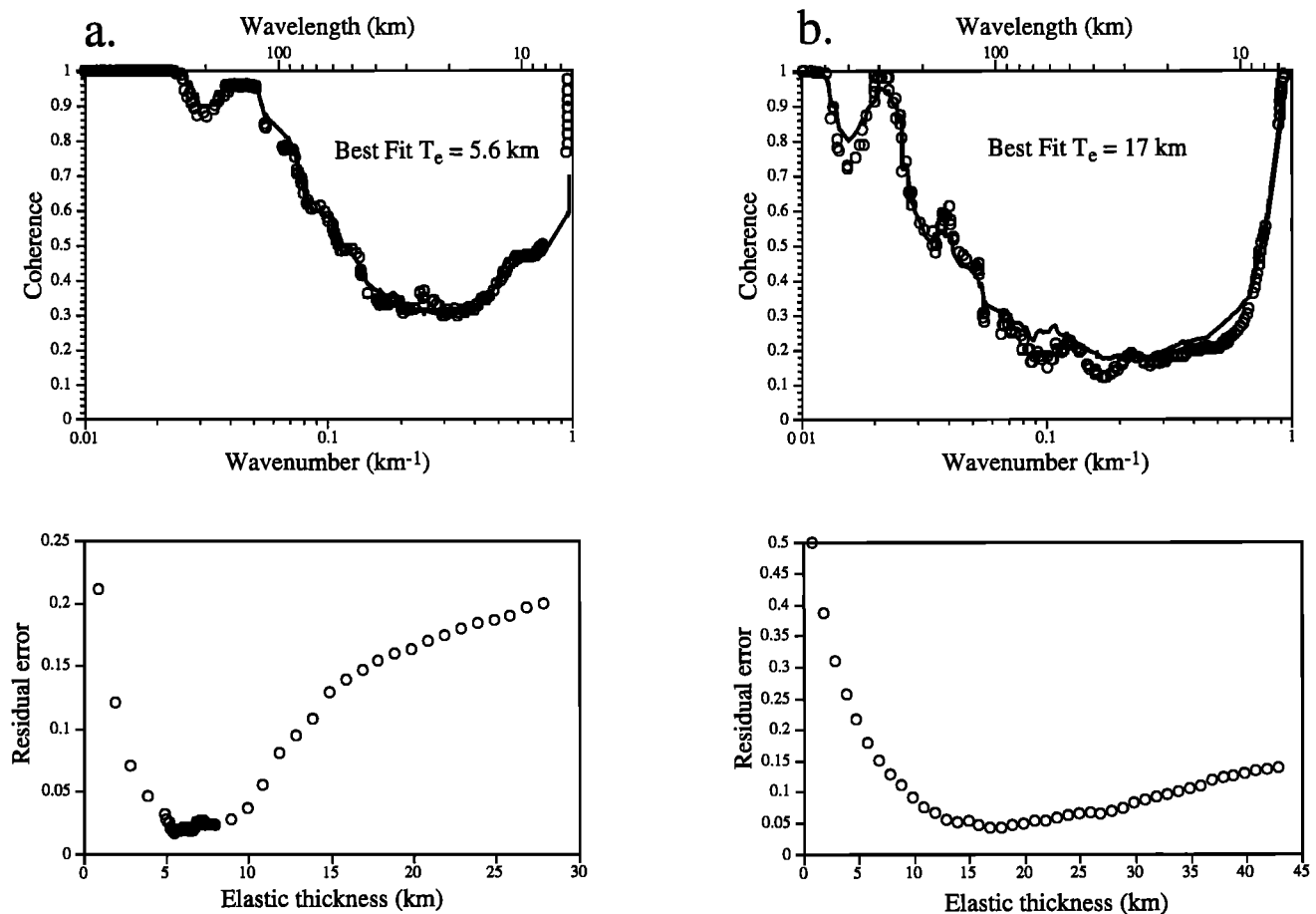[b]From *Braile et al.* [1982].
[c]From *Roller* [1965].

Figure 6. Examples of observed (open circles) and best fit predicted (solid line) coherence functions, along with plots of residual error, from (a) the northwest corner of the study area and (b) the southeast corner.

province, exhibits low rigidity as well (1.6×10^{21} to 7.4×10^{21} N m; $T_e = 5.6$ to 9.4 km). The Colorado Plateau is typified by higher rigidity than the adjacent Basin and Range, 3.0×10^{22} to 4.1×10^{23} N m ($T_e = 15$ to 36 km), with mean 9×10^{22} N m ($T_e = 22$ km) and median error limits 2×10^{22} to 4×10^{23} N m ($T_e = 13$ to 36 km). The greatest flexural strength is observed in the Middle Rocky Mountains province, where estimates are from 2.0×10^{22} to 4.1×10^{24} N m ($T_e = 13$ to 77 km) and mean rigidity is 3×10^{23} N m ($T_e = 33$ km) with median error limits 4×10^{22} to 3×10^{24} N m ($T_e = 16$ to 68 km).

These results compare favorably with most independent determinations of flexural rigidity in the region. For example, two-dimensional modeling of loading by low-angle thrust faulting and associated foreland basins [*Jordan*, 1981] indicates a flexural rigidity of $\sim 10^{23}$ N m ($T_e \cong 22$ km) associated with the Meade thrust event, denoted MT in Plate 2a. Because *Jordan* [1981] modeled basins formed during Sevier thrusting, her result should document the rigidity of the elastic layer during the mid-Cretaceous rather than at present, but nevertheless, her estimate is consistent with the range of flexural rigidity that we observe in the area (6×10^{22} to 4×10^{23} N m; $T_e = 19$ to 36 km). *Londe* [1986] employed an admittance technique to assess flexural rigidity along the Basin and Range–Colorado Plateau transition at $\sim 10^{20}$–10^{21} N m ($T_e \sim 2.2$–4.8 km). Bearing in mind that inversion of the admittance function emphasizes the flexurally weakest portions of a domain [*Forsyth*, 1985], *Londe*'s [1986] upper bound is consistent with our

smallest estimate from the Basin and Range (D = 9×10^{20} N m; $T_e = 4.6$ km). *Bechtel* [1989] used periodogram coherence analysis in windows designed to approximately isolate the Basin and Range and Colorado Plateau provinces, finding rigidities of 1×10^{21} (4.9 km) and 5×10^{22} N m (18 km), respectively. Those results are virtually identical to the lowest rigidities reported here for corresponding provinces. Finally, modeling of local uplift on Basin and Range normal faults [*King and Ellis*, 1990] indicates that associated flexural rigidity should be of order 7×10^{19} to 6×10^{20} N m ($T_e = 2$ to 4 km), for which the upper bound is consistent with our lowest Basin and Range values. Modeling of the Wasatch fault in particular [*Zandt and Owens*, 1980] suggests flexural rigidity in the footwall of 6×10^{21} to 4×10^{22} N m ($T_e = 9$ to 17 km); again, the upper bound is consistent with our lowest values from that area.

Discussion

There is one independent assessment of flexural rigidity that is decidedly inconsistent with our results. Several investigators [*Walcott*, 1970b; *Passey*, 1981; *Nakiboglu and Lambeck*, 1983; *Bills and May*, 1987] have reported flexural rigidities ranging from 5×10^{22} to 2×10^{23} N m ($T_e = 18$ to 30 km) for the rebound of the Pleistocene Lake Bonneville, as modeled from measurements of relative elevation of lake shore terraces. These numbers are much greater than the rigidities we
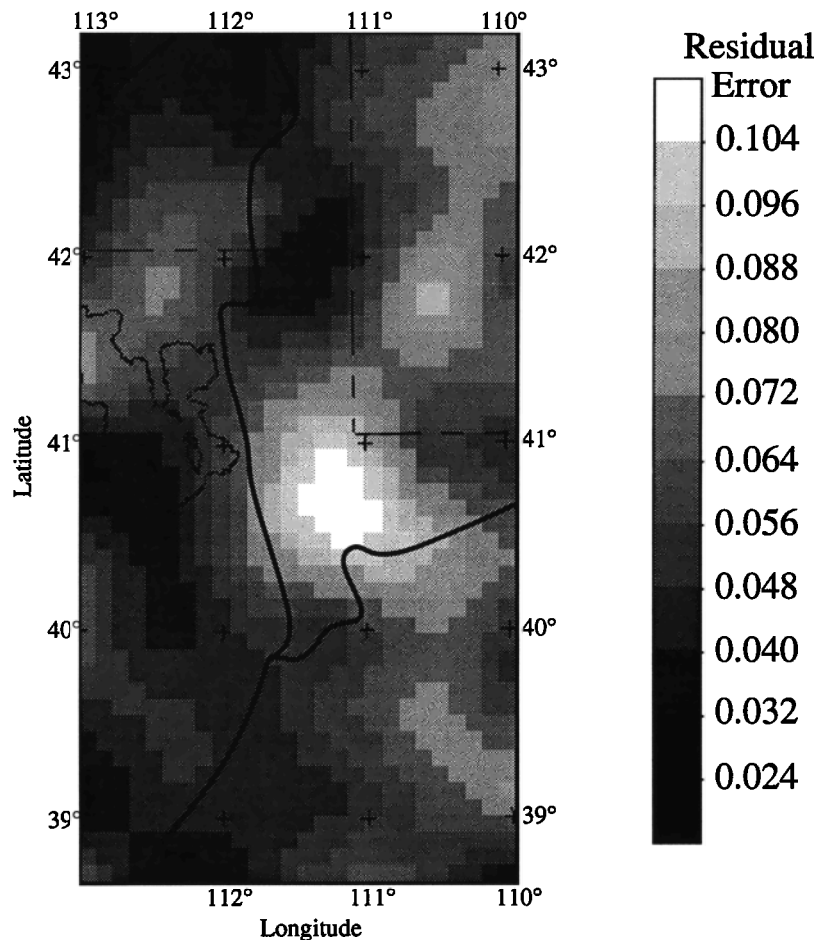
Figure 7. Interpolated contour of residual error (predicted minus observed coherence).

have determined for the same location of 9×10^{20} to 4×10^{22} N m; $T_e = 4.6$ to 16 km (Plate 2a). There are two possible explanations for the discrepancy. The first possibility is that crustal temperatures were much greater in the past (say, for example, the mid-Miocene, ~15 Ma), and the Basin and Range load structure was emplaced prior to that time; that is, there has been negligible erosional-depositional or tectonic redistribution in the time since. In that case, the flexural rigidity indicated by the coherence method would reflect an ancient rather than modern temperature field [e.g., *Courtney and Beaumont*, 1983]. In effect, it would record a fossil flexural rigidity. However, evidence for many tens of kilometers of approximately east-west extension since 15 Ma in the easternmost Basin and Range [e.g., *Wernicke et al.*, 1987] suggests that the load structure of the easternmost Basin and Range has not remained unchanged for enough time to reflect a radically different crustal geotherm.

Alternatively, one may note that all of the Lake Bonneville rebound studies model viscoelastic isostatic response of the lithosphere, and all infer that the elastic layer achieved isostatic equilibrium both during loading (a < 15 kyr time span) and after the load was removed (~11 ka). Although some studies used models capable of describing a rheologically stratified Earth such as that postulated by *Smith and Bruhn* [1984], none of the investigations explored the possibility of a viscoelastic lower crust. The probable reason for omission of the lower crust from the calculations is that containment of viscoelastic

fluid in a thin channel dramatically increases the isostatic response time [*Nakiboglu and Lambeck*, 1983]. Thus while the lithosphere indeed achieved isostatic equilibrium with respect to viscosities of the upper mantle ductile zone, it probably was not loaded sufficiently long to achieve isostatic equilibrium with respect to a lower crustal ductile zone sandwiched between crustal and upper mantle elastic layers. *Willett et al.* [1984, 1985] modeled the temporal evolution of viscoelastic flexural response in a rheologically stratified lithosphere and found that the apparent elastic thickness strongly depends on duration of the load. In that study, continental lithosphere having surface heat flow 90 mW m^{-2} exhibited rigidity of 2×10^{23} N m ($T_e = 30$ km) after 10^4 years as compared to 5×10^{22} N m ($T_e = 18$ km) after 10^6 years, following relaxation of stresses in the lower crust. Since most of the load structure described by coherence analysis has resided for ~10^6 to 10^8 years, as compared to 10^4 years for Lake Bonneville, the observed discrepancy would be expected.

Correlation With Heat Flow and Tectonism

Flexural rigidity in the Basin and Range–Colorado Plateau–Middle Rocky Mountains transition exhibits remarkable spatial correlation with a number of geologic and geophysical features. There are strong relationships with surface heat flow, with age and tectonic history of the continental lithosphere, and with locations of Cenozoic normal faults that have experienced large displacements. More subtle relationships seem to

occur between rigidity and secondary fault structures such as segmentation of the late Cenozoic Wasatch normal fault zone and displacement transfer structures associated with Cretaceous/early-Tertiary low-angle reverse faults.

Where regional heat flow is well determined, low flexural rigidity corresponds with high heat flow (compare Plates 2a and 2b). This result is expected because rigidity depends most heavily on power law creep of rocks, which depends in turn on temperature and composition. The correlation is most readily apparent in the western half of the study area. Highest heat flow, > 100 mW m^{-2}, characterizes the eastern Snake River Plain, where the lithosphere was thermally perturbed by passage of the Yellowstone hotspot around 10 Ma, and the province correspondingly exhibits very low flexural rigidity. Heat flow is also high (90–100 mW m^{-2}) in the flexurally weak Great Salt Lake and Sevier Desert regions of the Basin and Range. Inside the 1.4 Ga isotopic age contour, Basin and Range heat flow is interpreted to be slightly less, 80–90 mW m^{-2}, and flexural rigidity is correspondingly greater. Heat flow and flexural rigidity also correlate with post-mid-Miocene extension of the eastern Basin and Range; many tens of kilometers of extension have occurred in the Great Salt Lake and Sevier Desert regions, decreasing to less than 10 km farther north [e.g., Wernicke et al., 1987].

Heat flow is much lower in the northwestern Colorado Plateau and Middle Rocky Mountains than in the Basin and Range, corresponding to much higher flexural rigidity, but smaller-scale correlation is not apparent within the eastern provinces. The cold thermal interior and transitionally higher heat flow thermal periphery of the Colorado Plateau, as described by Bodell and Chapman [1982], is not apparent in the flexural rigidity estimates. Moreover, few measurements describe heat flow in the Middle Rocky Mountains province where flexural rigidity is greatest. However, the most rigid portion of the Middle Rocky Mountains province ends abruptly at the 1.4 Ga K-Ar biotite age contour that defines the Archean Wyoming craton (Plate 2a). Many investigators observe low surface heat flow over cratons, which they suggest results from refraction of deep mantle heat around a devolatilized Archean lithospheric root [e.g., Ballard and Pollack, 1988; Nyblade and Pollack, 1992]. Hence the Archean Wyoming craton might be expected to have relatively low heat flow despite thermal overprinting by recent tectonism.

The persistence of the tectonic boundary at the eastern limit of the Basin and Range, over hundreds of millions of years and through multiple tectonic events, argues strongly that inherited characteristics of the lithosphere influence the modern distribution of tectonism. Lower thermal conductivity is expected to cause thermal refraction of deep mantle heat around the Archean lithosphere of the Wyoming province, and hence reduced heat flow. Devolatilization of mantle rock probably contributes to lowered ductility of the upper mantle as well [Pollack, 1986], and in addition to increasing the flexural rigidity, the resulting inhibition of advective heat transfer may further reduce heat flow. Hence the relationship of continental lithosphere genesis to flexural rigidity and heat flow properties may be in large part a function of minor variations in bulk composition.

The transition from low to high flexural rigidity also exhibits an apparent correlation with the easternmost occurrence of Cenozoic normal faults with large displacements (Plate 3a). The coincidence of major normal faults and low rigidity may

be explained in either of two possible ways: (1) major faults are directly responsible for weakening of the elastic layer, or (2) lithospheric characteristics that determine the variation of flexural rigidity independently control the geometry and distribution of faulting as well. As an example of the first case, if fractures extend all the way through the elastic layer and can serve as discontinuities in stress behavior, they could reduce flexural rigidity by promoting "broken plate" behavior, for which the isostatic response would resemble that of a much weaker continuous media [e.g., Walcott, 1970a]. However, fault-bounded blocks in the Basin and Range are supported entirely by the strength of the plate rather than rotational isostasy or other isostatic mechanisms [Eaton et al., 1978; Bechtel, 1989], so "broken plate" behavior is deemed unlikely.

Plate-bending stresses resulting from footwall flexure are likely contributors to reduced flexural strength, however [e.g., Zandt and Owen, 1980]. In-plane (or tectonic) stresses can also reduce flexural strength as a result of failure within a depth-dependent yield strength envelope [McNutt and Menard, 1982], and hence the correlation with faulting might also be traced to the stress regime which activated the faults in the first place. On the other hand, the long-term persistence of the tectonic boundary implies that the relationship between rigidity and faulting is at least partially a function of independent control by other factors, such as variations in bulk composition of the lithosphere (translating to variations in the retardation of heat flow). Consequently, neither of the proposed explanations for the relationship of flexural strength to faulting can be ruled particularly unlikely.

Flexural rigidity appears to correlate with other characteristics of faulting as well. For example, there is a correlation of rigid blocks in the Middle Rocky Mountains (Plate 3a) with proposed segmentation of the 370-km-long, late Cenozoic Wasatch fault [e.g., Schwartz and Coppersmith, 1984]. Also, the easternmost exposure of low-angle thrust sheets associated with the Laramide and Sevier orogenies (Plate 3b) occurs, in general, 0 to 100 km east of the flexural strength transition. Other studies have suggested that the final location of thin skin deformation fronts may be defined by mechanical coupling to cratonic lithosphere of the Indian shield south of the Himalayas [Lyon-Caen and Molnar, 1985], and the Brazilian shield east of the Bolivian Andes [Lyon-Caen et al., 1985], at distances of 100 to 200 km from the leading edge of the craton. Displacement transfer structures in thin skin thrusts also correspond to local maxima of flexural rigidity along a north-south transect. Note, however, that the Uinta arch transfer structures have been exaggerated by subsequent folding, thrusting and erosion during the Laramide compressional event that formed the Uinta mountains [Bruhn et al., 1986].

It is not surprising that secondary structures of large faults should indicate a relationship with flexural rigidity. In the case of Wasatch fault segmentation, a differential isostatic response to unloading of the footwall block along the length of the fault should evolve a recognizable variation in geomorphic and geometric expression over its ~18 m.y. history. Similarly, in the case of low-angle thrust sheets advancing from an elastically weak accretionary terrane to a stronger area of cratonic or epicratonic origin, differential isostatic response of the craton to loading by the thrust sheets might play a role in determining where thrusts advance the furthest and, consequently, where displacement transfer structures are likely to be found.
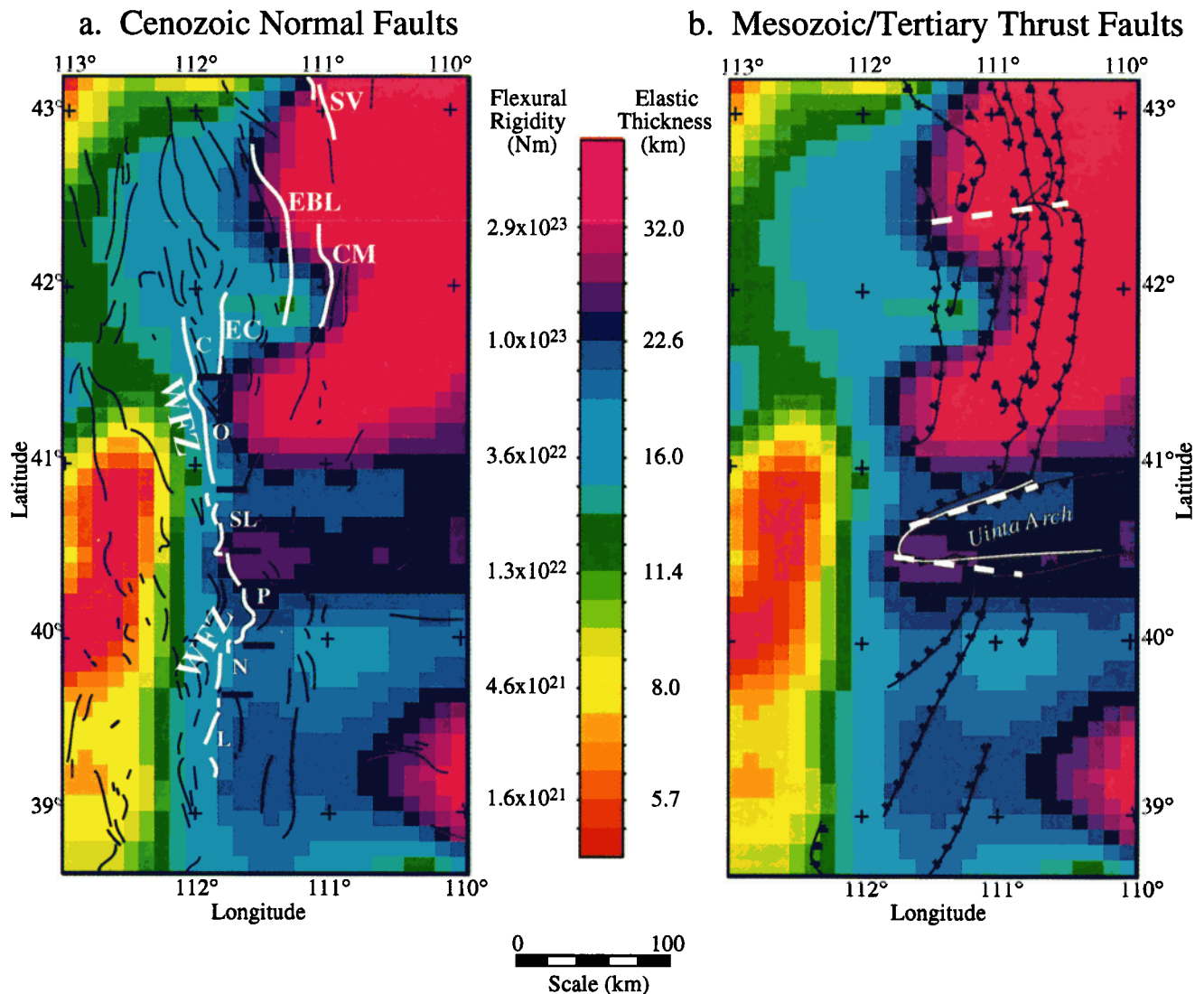
a. Cenozoic Normal Faults

b. Mesozoic/Tertiary Thrust Faults

Plate 3. Relationship of flexural rigidity to Cenozoic normal faults and Cretaceous–Tertiary overthrusts. (a) Flexural rigidity and surface traces of normal faults exhibiting late Quaternary (<500 ka) surface rupture [after *Hecker* 1993; *Smith and Arabasz*, 1991]. The easternmost faults with significant (> 1 km) offset are indicated in bold white pen. Faults are CM, Crawford Mountains; EBL, East Bear Lake; EC, East Cache; SV, Star Valley; WFZ, Wasatch fault zone. Segmentation of the Wasatch fault is after *Schwartz and Coppersmith* [1984]: C, Collinston; L, Levan; N, Nephi; O, Ogden; P, Provo; SL, Salt Lake. (b) Flexural rigidity and Cretaceous/Tertiary overthrusts [after *Blackstone*, 1977; *Hintze*, 1980]. Locations of displacement transfer structures are emphasized by dashed white lines.

Conclusions

In this paper, a methodology is developed for stochastic inversion of flexural rigidity using a maximum entropy-based approach to coherence analysis. This methodology is employed to map large variations in the Earth's isostatic response with greater resolution than was previously possible. Flexural rigidity in the easternmost Basin and Range is found to average 9×10^{21} N m ($T_e = 10$ km) and varies from 8.7×10^{20} to 3.6×10^{22} N m ($T_e = 4.6$ to 16 km). Rigidity of the northwestern Colorado Plateau ranges from 3.0×10^{22} to 4.1×10^{23} N m ($T_e = 15$ to 36 km) and averages 9×10^{22} N m ($T_e = 22$ km). Flexural rigidity of the Middle Rocky Mountains averages 3×10^{23} N m ($T_e = 33$ km) and can range from 2.0×10^{22} to 4.1×10^{24} N m ($T_e = 13$ to 77 km). These results compare favor-

ably with independent estimates of flexural rigidity from modeling of individual features and periodogram stochastic inversion using much larger windows, with the exception of determinations from modeling of the Lake Bonneville rebound. The latter discrepancy may indicate a viscoelastic lower crustal zone of flexural decoupling which did not respond isostatically to the short-lived Lake Bonneville load but has responded to more enduring loads.

The mapped variation of flexural rigidity is supported by correlations with independent geologic and geophysical information. Low flexural rigidity is strongly correlated with high surface heat flow, as predicted by the relationship between strength of the elastic layer and the temperature-dependent ductile flow law. The elastic layer is very rigid in the Archean Wyoming craton, where heat flow is poorly con-

strained but is probably relatively low as is observed in other cratonic regions. Relationships are also apparent between flexural rigidity and the locations of displacement transfer structures in Mesozoic overthrusts, as well as segment boundaries on the Wasatch fault. In addition, the distribution of Cenozoic normal faults with large displacements is strongly correlated to regions of low flexural rigidity, implying a genetic relationship between faulting and rigidity.

Appendix: Load Deconvolution for an Arbitrary Density Profile

Following *Forsyth's* [1985] derivation, consider a thin elastic plate having density $\rho = \rho_0$ at the top (the Earth's surface, $z = 0$), $\rho = \rho_1$ at the base (depth $z = h$), and a one-dimensional (but otherwise arbitrary) density distribution $\rho(z)$ between (Figure 2a). A topographic load atop the plate with initial Fourier amplitude $H_I(k)$ (Figure 2b) will induce a deflection $W_T(k)$ to achieve flexural isostasy (Figure 2c). The resulting topography will have amplitude $H_T(k)$ given by

$$H_T(k) = H_I(k) + W_T(k). \tag{A1}$$

The amplitude of the Bouguer anomaly $B_T(k)$ corresponding to the flexure $W_T(k)$ is given by

$$B_T(k) = \left[2\pi G \int_0^h \frac{d\rho}{dz} \exp(-kz)\,dz \right] W_T(k) \tag{A2}$$

where G is the gravitational constant. The relationship between amplitude of the resulting topography and amplitude of the compensating deflection is given by

$$W_T(k) = -\frac{\rho_0}{\rho_1 - \rho_0 + \dfrac{D}{g} k^4} H_T(k), \tag{A3}$$

in which D is flexural rigidity of the plate and g is gravitational acceleration.

If a subsurface load with initial amplitude $W_I(k)$ and density contrast $\Delta\rho_L$ is introduced at a depth z_L, flexural isostatic response will produce topography of amplitude $H_B(k)$ (Figure 2c). The final expression of the density contrast at z_L will have amplitude $W_B(k)$:

$$W_B(k) = W_I(k) + H_B(k). \tag{A4}$$

The resulting Bouguer gravity anomaly will be

$$B_B(k) = \left\{ 2\pi G \left[\int_0^h \frac{d\rho}{dz} \exp(-kz)\,dz \right. \right.$$
$$\left. \left. - \left(\rho_1 + \frac{D}{g} k^4\right) \exp(-kz_L) \right] \right\} H_B(k) \tag{A5}$$

with

$$H_B(k) = -\frac{\Delta\rho_L}{\rho_1 - \Delta\rho_L + \dfrac{D}{g} k^4} W_B(k). \tag{A6}$$

If loads at the surface and at depth are in phase, i.e., spatially correlated, the observed topographic amplitude is thus given by

$$H(k) = H_T(k) + H_B(k) \tag{A7}$$

and the Bouguer anomaly will have Fourier amplitude:

$$B(k) = B_T(k) + B_B(k). \tag{A8}$$

However, it is expected that surface and subsurface loading are not in phase. Hence these operations are performed separately for the real and imaginary parts of the complex Fourier amplitudes. Substitution gives the topographic amplitude to be

$$H(k) = \left[\frac{\rho_1 - \rho_0 + \dfrac{D}{g} k^4}{\rho_1 + \dfrac{D}{g} k^4} \right] H_I(k) - \left[\frac{\Delta\rho_L}{\rho_1 + \dfrac{D}{g} k^4} \right] W_I(k) \tag{A9}$$

and the harmonic of the Bouguer anomaly is

$$B(k) = \left[\frac{-2\pi G \rho_0 \displaystyle\int_0^h \frac{d\rho}{dz} \exp(-kz)\,dz}{\rho_1 + \dfrac{D}{g} k^4} \right] H_I(k)$$

$$- \left\{ 2\pi G \Delta\rho_L \left[\frac{\displaystyle\int_0^h \frac{d\rho}{dz} \exp(-kz)\,dz}{\rho_1 + \dfrac{D}{g} k^4} - \frac{\exp(-kz_L)}{\Delta\rho_L} \right] \right\} W_I(k). \tag{A10}$$

The above system of equations is solved for the initial applied loads H_I and W_I. Then the topography and gravity amplitudes are deconvolved into their respective components via

$$H_T(k) = \left[\frac{\rho_1 - \rho_0 + \dfrac{D}{g} k^4}{\rho_1 + \dfrac{D}{g} k^4} \right] H_I(k)$$

$$H_B(k) = H(k) - H_T(k)$$

$$B_B(k) = \left\{ -2\pi G \Delta\rho_L \left[\frac{\displaystyle\int_0^h \frac{d\rho}{dz} \exp(-kz)\,dz}{\rho_1 + \dfrac{D}{g} k^4} - \exp(-kz_L) \right] \right\} W_I(k) \tag{A11}$$

$$B_T(k) = B(k) - B_B(k).$$

References

Airy, G. B., On the computation of the effect of the attraction of mountain-masses as disturbing the apparent astronomical latitude of stations of geodetic surveys, *Philos. Trans. R. Soc.*, *145*, 101–104, 1855.

Anderson, R. E., Tectonic evolution of the Intermontane system: Basin and Range, Colorado Plateau, and High Lava Plains, in Geophysical Framework of the Continental United States, edited by L. C. Pakiser and W. D. Mooney, *Mem. Geol. Soc. Am.*, *172*, 162–176, 1989.

Ballard, S., and H. N. Pollack, Modern and ancient geotherms beneath southern Africa, *Earth Planet. Sci. Lett.*, *88*, 132–142, 1988.

Banks, R. J., R. L. Parker, and S. P. Huestis, Isostatic compensation on a continental scale: Local versus regional mechanisms, *Geophys. J. R. Astron. Soc.*, *51*, 431–452, 1977.

Barrell, J., The strength of the Earth's crust, 8, Physical conditions controlling the nature of lithosphere and asthenosphere, *J. Geol.*, *22*, 425–433, 1914.

Barton, P. J., The relationship between seismic velocity and density in the continental crust— a useful constraint?, *Geophys. J. R. Astron. Soc.*, *87*, 195–208, 1986.

Bechtel, T. D., Mechanisms of isostatic compensation in East Africa and North America, Ph.D. dissertation, 247 pp., Brown Univ., Providence, R. I., 1989.

Bechtel, T. D., D. W. Forsyth, and C. J. Swain, Mechanisms of isostatic compensation in the vicinity of the East African Rift, Kenya, *Geophys. J. R. Astron. Soc.*, *90*, 445–465, 1987.

Bechtel, T. D., D. W. Forsyth, V. L. Sharpton, and R. F. Grieve, Variations in effective elastic thickness of the North American lithosphere, *Nature*, *343*, 636–638, 1990.

Beghoul, N., and M. Barazangi, Mapping high P_n velocity beneath the Colorado plateau constrains uplift models, *J. Geophys. Res.*, *94*, 7083–7104, 1989.

Bills, B. G., and G. M. May, Lake Bonneville: Constraints on lithospheric thickness and upper mantle viscosity from isostatic warping of Bonneville, Provo and Gilbert stage shorelines, *J. Geophys. Res.*, *92*, 11,493–11,508, 1987.

Bird, P., Lateral extrusion of lower crust from under high topography, in the isostatic limit, *J. Geophys. Res.*, *96*, 10,275–10,286, 1991.

Black, R. A., Suppression of dominant topographic overprints in gravity data by adaptive filtering: Southern Wyoming Province, *J. Geophys. Res.*, *97*, 14,237–14,243, 1992.

Blackman, D. K., and D. W. Forsyth, Isostatic compensation of tectonic features of the Mid-Atlantic Ridge: 25°–27°30'S, *J. Geophys. Res.*, *96*, 11,741–11,758, 1991.

Blackstone, D. L., The overthrust salient of the Cordilleran fold belt, western Wyoming–southeastern Idaho–northeastern Utah, in *Twenty-Ninth Annual Field Conference Guidebook*, Wyoming Geological Association, pp. 367–384, Casper, 1977.

Blackwell, D. D., and J. L. Steele, Geothermal map of North America, scale 1:5,000,000, Geol. Soc. of Am., Boulder, Colo., 1992.

Bodell, J.M., and D. S. Chapman, Heat flow in the north central Colorado Plateau, *J. Geophys. Res.*, *87*, 2869–2884, 1982.

Braile, L. W., R. B. Smith, G. R. Keller, R. M. Welch, and R. P. Meyer, Crustal structure across the Wasatch Front from detailed seismic refraction studies, *J. Geophys. Res.*, *79*, 2669–2677, 1974.

Braile, L. W., R. B. Smith, J. Ansorge, M. R. Baker, M. A. Sparlin, C. Prodehl, M. M. Schilly, J. H. Healy, St. Mueller, and K. H. Olsen, The Yellowstone-Snake River Plain seismic profiling experiment: Crustal structure of the eastern Snake River Plain, *J. Geophys. Res.*, *87*, 2597–2609, 1982.

Bruhn, R. L., M. D. Picard, and J. S. Isby, Tectonics and sedimentology of the Uinta arch, western Uinta mountains, and Uinta basin, in Paleotectonics and Sedimentation, edited by J. A. Peterson, *AAPG Mem.*, *41*, 333–352, 1986.

Buck, W. R., Flexural rotation of normal faults, *Tectonics*, *7*, 959–973, 1988.

Burchfiel, B. C., and G. A. Davis, Nature and controls of Cordilleran orogenesis, western United States: Extensions of an earlier synthesis, *Am. J. Sci.*, *275A*, 363–396, 1975.

Burg, J. P., Maximum entropy spectral analysis, Ph.D. dissertation, Stanford Univ., Stanford, Calif., 1975.

Caldwell, J. G., W. F. Haxby, D. E. Karig, and D. L. Turcotte, On the applicability of a universal elastic trench profile, *Earth Planet. Sci. Lett.*, *31*, 239–246, 1976.

Chery, J., F. Lucazeau, M. Daigneres, and J. P. Vilotte, Large uplift of rift flanks: A genetic link with lithospheric rigidity?, *Earth Planet. Sci. Lett.*, *112*, 195–211, 1992.

Condie, K. C., *Archean Greenstone Belts*, Elsevier Scientific, New York, 1981.

Courtney, R. C., and C. Beaumont, Thermally-activated creep and flexure of the oceanic lithosphere, *Nature*, *305*, 201–204, 1983.

Dorman, L. M., and B. T. R. Lewis, Experimental isostasy, 1, Theory of the determination of the earth's isostatic response to a concentrated load, *J. Geophys. Res.*, *75*, 3357–3366, 1970.

Dorman, L. M., and B. T. R. Lewis, Experimental isostasy, 3, Inversion of the isostatic Green function and lateral density changes, *J. Geophys. Res.*, *77*, 3068–3077, 1972.

Eaton, G. P., R. R. Wahl, H. J. Prostka, D. R. Mabey, and M. D. Kleinkopf, Regional gravity and tectonic patterns: Their relation to late Cenozoic epeirogeny and lateral spreading in the western Cordillera, in Cenozoic Tectonics and Regional Geophysics of the Western Cordillera, edited by R. B. Smith and G. P. Eaton, *Mem. Geol. Soc. Am.*, *152*, 51–91, 1978.

Forsyth, D. W., Subsurface loading and estimates of the flexural rigidity of continental lithosphere, *J. Geophys. Res.*, *90*, 12,623–12,632, 1985.

Gunn, R., A quantitative evaluation of the influence of the lithosphere on the anomalies of gravity, *J. Franklin Inst.*, *236*, 47–65, 1943.

Haxby, W. F., D. L. Turcotte, and J. M. Bird, Thermal and mechanical evolution of the Michigan Basin, *Tectonophysics*, *36*, 57–75, 1976.

Hecker, S., Quaternary tectonics of Utah with emphasis on earthquake-hazard characterization, *Utah Geol. Surv. Bull.*, *127*, 157 pp., 1993.

Hintze, L. F., Geologic map of Utah, scale 1:500,000, Utah Geol. Mineral Surv., Salt Lake City, 1980.

Humphreys, E. D., and K. G. Dueker, Western U.S. upper mantle structure, *J. Geophys. Res.*, *99*, 9615–9634, 1994.

Jaynes, E. T., Where do we go from here?, in *Maximum Entropy and Bayesian Methods in Inverse Problems*, edited by C. R. Smith and W. T. Grandy, pp. 21–58, D. Reidel, Norwell, Mass., 1985.

Jones, C. H., B. P. Wernicke, G. L. Farmer, J. D. Walker, D. S. Coleman, L. W. McKenna, and F. V. Perry, Variations across and along a major continental rift: An interdisciplinary study of the Basin and Range Province, western USA, *Tectonophysics*, *213*, 57–96, 1992.

Jordan, T. E., Thrust loads and foreland basin evolution, Cretaceous, western United States, *AAPG Bull.*, *65*, 2506–2520, 1981.

Karlstrom, K. E., and R. S. Houston, The Cheyenne belt: Analysis of a Proterozoic suture in southern Wyoming, *Precambrian Res.*, *25*, 415–446, 1984.

Karner, G. D., and A. B. Watts, Gravity anomalies and flexure of the lithosphere at mountain ranges, *J. Geophys. Res.*, *88*, 10449–10477, 1983.

Kay, S. M., *Modern Spectral Estimation*, Prentice-Hall, Englewood Cliffs, N. J., 1988.

Kay, S. M., and S. L. Marple, Spectrum analysis–A modern perspective, *Proc. IEEE, 69*, 1380–1419, 1981.

King, G., and M. Ellis, The origin of large local uplift in extensional regions, *Nature, 348*, 689–693, 1990.

Lewis, B. T. R., and L. M. Dorman, Experimental isostasy, 2, An isostatic model for the United States derived from gravity and topographic data, *J. Geophys. Res., 75*, 3367–3386, 1970.

Lim, J. S., and N. A. Malik, A new algorithm for two-dimensional maximum entropy power spectrum estimation, *IEEE Trans. Acoust. Speech Signal Process., 29*, 401–413, 1981.

Lipman, P. W., H. J. Prostka, and R. L. Christiansen, Cenozoic volcanism and plate-tectonic evolution of the western United States, 1, Early and middle Cenozoic, *Philos. Trans. R. Soc. London A, 271*, 217–248, 1972.

Londe, M. D., The Colorado Plateau–Basin and Range transition zone in central Utah: Thermomechanical modeling and spectral analysis of topographic and gravity data, Ph.D. dissertation, 157 pp., Univ. of Wyo., Laramie, 1986.

Lowry, A. R., Flexural strength and stress in the Cordillera, western United States, Ph.D. dissertation, 105 pp., Univ. of Utah, Salt Lake City, 1994.

Ludwig, W. J., J. E. Nafe, and C. L. Drake, Seismic refraction, in *New Concepts of Sea Floor Evolution, Pt 1, Regional Observations, The Sea: Ideas and Observations on Progress in the Study of the Seas*, vol. 4, edited by A. E. Maxwell, pp. 53–84, Wiley-Interscience, New York, 1970.

Lyon-Caen, H., and P. Molnar, Constraints on the structure of the Himalaya from an analysis of gravity anomalies and a flexural model of the lithosphere, *J. Geophys. Res., 88*, 8171–8192, 1983.

Lyon-Caen, H., and P. Molnar, Gravity anomalies, flexure of the Indian plate, and structure, support, and evolution of the Himalaya and Ganga Basin, *Tectonics, 4*, 513–538, 1985.

Lyon-Caen, H., P. Molnar, and G. Suarez, Gravity anomalies and flexure of the Brazilian shield beneath the Bolivian Andes, *Earth Planet. Sci. Lett., 75*, 81–92, 1985.

Macario, A., A. Malinverno, and W. F. Haxby, On the robustness of elastic thickness estimates obtained using coherence methodology: Application to the Alps, *Eos Trans. AGU, 73 (43)*, Fall Meeting suppl., 571, 1992.

Malik, J. S., and N. A. Lim, Properties of two-dimensional maximum entropy power spectrum estimates, *IEEE Trans. Acoust. Speech Signal Process., 30*, 788–798, 1982.

McKenzie, D., Some remarks on the development of sedimentary basins, *Earth Planet. Sci. Lett., 40*, 25–32, 1978.

McKenzie, D., and C. Bowin, The relationship between bathymetry and gravity in the Atlantic Ocean, *J. Geophys. Res., 81*, 1903–1915, 1976.

McNutt, M. K., Influence of plate subduction on isostatic compensation in northern California, *Tectonics, 2*, 399–415, 1983.

McNutt, M. K., and H. W. Menard, Constraints on yield strength in the oceanic lithosphere derived from observations of flexure, *Geophys. J. R. Astron. Soc., 71*, 363–394, 1982.

Nakiboglu, S. M., and K. Lambeck, A reevaluation of the isostatic rebound of Lake Bonneville, *J. Geophys. Res., 88*, 10,439–10,447, 1983.

Nyblade, A. A., and H. N. Pollack, Heat flow from Archean and Proterozoic lithosphere, *Eos Trans. AGU, 73 (14)*, Spring Meeting suppl., 302, 1992.

O'Hara, N. W., and P. L. Lyons, New map updates gravity data, *Geotimes, 28*, 22–27, 1983.

Passey, Q. R., Upper mantle viscosity derived from the difference in rebound of the Provo and Bonneville shorelines: Lake Bonneville basin, Utah, *J. Geophys. Res., 86*, 11701–11708, 1981.

Pollack, H. N., Cratonization and thermal evolution of the mantle, *Earth Planet. Sci. Lett., 80*, 175–182, 1986.

Pratt, J. H., On the attraction of the Himalaya Mountains and of the el-

evated regions beyond them, upon the plumb line in India, *Philos. Trans. R. Soc. London, 145*, 53–100, 1855.

Roller, J. C., Crustal structure in the eastern Colorado Plateaus province from seismic-refraction measurements, *Bull. Seismol. Soc. Am., 55*, 107–119, 1965.

Schwartz, D. P., and K. J. Coppersmith, Fault behavior and characteristic earthquakes: Examples from the Wasatch and San Andreas fault zones, *J. Geophys. Res., 89*, 5681–5698, 1984.

Simpson, R. W., R. C. Jachens, R. J. Blakely, and R. W. Saltus, A new isostatic residual map of the conterminous United States with a discussion on the significance of isostatic residual anomalies, *J. Geophys. Res., 91*, 8348–8372, 1986.

Smith, C. R., and W. T. Grandy (Eds.), *Maximum Entropy and Bayesian Methods in Inverse Problems*, D. Reidel, Norwell, Mass., 1985.

Smith, R. B., and W. J. Arabasz, Seismicity of the Intermountain seismic belt, in *Neotectonics of North America, Decade Map*, vol. 1, edited by D. B. Slemmons, E. R. Engdahl, M. D. Zoback, and D. D. Blackwell, pp. 185–228, Geological Society of America, Boulder, Colo., 1991.

Smith, R. B., and R. L. Bruhn, Intraplate extensional tectonics of the eastern Basin-Range: Inferences on structural style from seismic reflection data, regional tectonics, and thermal-mechanical models of brittle-ductile deformation, *J. Geophys. Res., 89*, 5733–5762, 1984.

Smith, R. B., W. C. Nagy, K. A. Julander, J. J. Viveiros, C. A. Barker, and D. G. Gants, Geophysical and tectonic framework of the eastern Basin and Range–Colorado Plateau–Rocky Mountain transition, in *Geophysical Framework of the Continental United States*, edited by L. C. Pakiser and W. D. Mooney, *Mem. Geol. Soc. Am., 172*, 205–233, 1989.

Smylie, D. E., G. K. C. Clarke, and T. J. Ulrych, Analysis of irregularities in the Earth's rotation, *Methods Comput. Phys., 13*, 391–430, 1973.

Stewart, J. H., Basin-Range structure in western North America: A review, in *Cenozoic Tectonics and Regional Geophysics of the Western Cordillera*, edited by R. B. Smith and G. P. Eaton, *Mem. Geol. Soc. Am., 152*, 1–31, 1978.

Tucker, G. E., and R. L. Slingerland, Erosional dynamics, flexural isostasy, and long-lived escarpments: A numerical modeling study, *J. Geophys. Res.*, this issue.

Turcotte, D. L., and G. Schubert, *Geodynamics*, John Wiley & Sons, New York, 1982.

Walcott, R. I., Flexure of the lithosphere at Hawaii, *Tectonophysics, 9*, 435–446, 1970a.

Walcott, R. I., Flexural rigidity, thickness and viscosity of the lithosphere, *J. Geophys. Res., 75*, 3941–3954, 1970b.

Watts, A. B., An analysis of isostasy in the world's oceans, 1, Hawaiian-Emperor seamount chain, *J. Geophys. Res., 83*, 5989–6004, 1978.

Watts, A. B., and N. M. Ribe, On geoid heights and flexure of the lithosphere at seamounts, *J. Geophys. Res., 89*, 11,152–11,170, 1984.

Watts, A. B, and M. S. Steckler, Subsidence and tectonics of Atlantic-type continental margins, *Oceanol. Acta, 4*, 143–153, 1981.

Wernicke, B. P., and G. J. Axen, On the role of isostasy in the evolution of normal fault systems, *Geology, 16*, 848–851, 1988.

Wernicke, B. P., R. L. Christiansen, P. C. England, and L. J. Sonder, Tectonomagmatic evolution of Cenozoic extension in the North American Cordillera, in *Continental Extensional Tectonics*, edited by M. P. Coward, J. F. Dewey, and P. L. Hancock, *Geol. Soc. Spec. Publ. London, 28*, 203–221, 1987.

Wessel, P., Thermal stresses and the bimodal distribution of elastic thickness estimates of the oceanic lithosphere, *J. Geophys. Res., 97*, 14,177–14,193, 1992.

Willett, S. D., D. S. Chapman, and H. J. Neugebauer, Mechanical response of the continental lithosphere to loading: effect of thermal regimes, *Ann. Geophys., 2*, 679–688, 1984.

Willett, S. D., D. S. Chapman, and H. J. Neugebauer, A thermo-mechanical model of continental lithosphere, *Nature, 314*, 520–523, 1985.

Zandt, G., and T. J. Owens, Crustal flexure associated with normal faulting and implications for seismicity along the Wasatch Front, Utah, *Bull. Seismol. Soc. Am.*, *70*, 1501–1520, 1980.

Zoback, M. L., and M. D. Zoback, Tectonic stress field of the continental United States, in Geophysical Framework of the Continental United States, edited by L. C. Pakiser and W. D. Mooney, *Mem. Geol. Soc. Am.*, *172*, 523–539, 1989.

A. R. Lowry and R. B. Smith, Department of Geology and Geophysics, 717 W. C. Browning Building, University of Utah, Salt Lake City, UT 84112-1183. (e-mail: arlowry@moose.utah.edu)